nature communications

Article

https://doi.org/10.1038/s41467-025-64000-1

Supramolecular networks with high shear stiffening enabled by metal ion-mediated hydrogen bonding enhancement strategy

Received: 12 November 2024

Accepted: 4 September 2025

Published online: 08 October 2025

Check for updates

Zhuo Chen[1,7], Heng Chen[1,2,7], Yuxi Li[1,3], Binli Wang[1,4], Shuhan Chen[1,3], Zhi-Yan Chen[1], Qianhua Huang[1,5], Xue-Feng Yu[1,3,6] & Rui He[1,3]

Shear stiffening gel (SSG) with prominent rate-dependent mechanical properties is promising for impact protection, but conventional boron-based SSG suffers from toxicity and corrosion arising from boric acid. Here, we design a boron-free supramolecular dynamic reversible network of polytitanosiloxane (PTS) based on the metal-ion-mediated hydrogen bonding enhancement strategy. Different oxidation states of Ti atoms in the network influence the charge distribution of the adjacent hydroxyl groups (Ti-OH). The electrostatic potential of the H-bond donor and acceptor could be effectively modulated by the Ti^{4+} and Ti^{3+} cations, thereby enhancing the H-bond strength. The resulting PTS SSG exhibits exceptional shear stiffening (~2800 times, 0.1–100 Hz), negligible corrosion, and low cytotoxicity (Grade 1). The PTS SSG is further explored for impact protection materials and flexible mechanical sensors in practice. The hydrogen bonding enhancement strategy also paves the way for developing dynamic reversible networks to fabricate next-generation smart materials.

Shear-stiffening gel (SSG) is a class of smart materials, in which the modulus or viscosity increases significantly with the increase of the external strain rate[1,2]. Due to this stimuli-responsive effect, SSG has great potential for use in protective gear, anti-impact devices[3,4] and rate sensors[5,6], which has attracted increasing attention in recent years. The common SSG is homogeneous polyborosiloxane (PBS) rubber with a low cross-linking degree, which is usually produced by crosslinking polydimethylsiloxane (PDMS) with boric acid (BA) at a high temperature, typically 180-220 °C[7]. The dynamic reversible interaction of a B-O cross bond is formed between two polymer chains by introducing B atoms into the polymer chains. On this basis, due to the shear rate-dependent characteristic of the B-O cross bond, PBS exhibits a typical shear stiffening effect by phase transition among the plastic, elastic, and glass states with the altering of external loading conditions[8]. However, BA has been well-known for its corrosion to steel and concrete, and the corrosion rate increases under higher temperatures[9,10]. There is a high risk of BA causing corrosion to production equipment during the manufacturing process. Furthermore, skin exposure to BA has been proven fatal, which was evidenced by many toxic experiments on animals[11–13]. The corrosion and toxicity of BA trigger security concerns limiting the applications of SSG in many fields. Therefore, it is highly urgent to develop a next generation of BA-free SSG.

The introduction of H-bond interaction into supramolecular networks to replace the B-O cross bonds has great potential to impart

[1]Materials Artificial Intelligence Center, Shenzhen Institutes of Advanced Technology, Chinese Academy of Sciences, Shenzhen, Guangdong, China. [2]Research Institute of Interdisciplinary Science, School of Materials Science and Engineering, Dongguan University of Technology, Dongguan, Guangdong, China. [3]University of Chinese Academy of Sciences, Beijing, China. [4]Key Laboratory of Micro-Nano Powder and Advanced Energy Materials of Anhui Higher Education Institutes, Anhui Engineering Research Center of Highly Reactive Micro-Nano Powders, Chizhou University, Chizhou, Anhui, China. [5]Science and Technology Institute of Advanced Technology, Wuhan, Hubei, China. [6]The Key Laboratory of Biomedical Imaging Science and System, Shenzhen Institutes of Advanced Technology, Chinese Academy of Sciences, Shenzhen, Guangdong, China. [7]These authors contributed equally: Zhuo Chen, Heng Chen. e-mail: rui.he1@siat.ac.cn

intelligent gels with desirable dynamic properties and stimuli-responsive characteristics[14,15]. To construct H-bonds in the polymer networks, polar groups could be incorporated into polymer chains through copolymerization or functionalization methods, which helps enhance intermolecular interactions[16]. However, this enhancement is still insufficient to impart the desired shear stiffening properties of PDMS. To overcome this problem, modulating the electrostatic potential of H-bond donor/acceptor to strengthen H-bonds constitutes an effective method[17–20]. Multivalent metals such as Ti, Fe, Cu, etc. exist in various ionic forms due to the distributions of their outer electrons[21,22]. High-valent metal ions can acquire electrons to be reduced to the lower oxidation state in certain catalysis processes[23–26]. Consequently, multivalent metals have the potential to modulate the electrostatic potential of adjacent M-OH by changing their oxidation state, which may be an effective strategy for enhancing H-bonds strength[27]. Unfortunately, although multivalent metal ions have already been exploited for battery, capacitor, and chemical catalyzation processes[21,26,28], the exploration of strengthening H-bond interactions in dynamic reversible networks of SSG remains untapped.

In this work, we propose a strategy that utilizes the variable-valence metal ion to adjust the electrostatic potential of the H-bond donor and acceptor, thereby enhancing the strength of H-bonds in supramolecular networks. Experimentally, we synthesize alkoxysilane-modified PDMS, which can hydrolyze and condense with metal coupling agents (Fig. 1a). We select tetra-isopropyl titanate (TTIP) as a metal coupling agent example to construct dynamic reversible networks that support the stable coexistence of Ti^{4+} and Ti^{3+} oxidation states. Compared with normal Si-OH, the charge density of the O atom in the Ti^{3+}-OH is denser and the charge density of the H atom in the Ti-OH is scarcer (Fig. 1b). As such, the Si-O-Ti heterogeneous structure can acquire strengthened H-bond interactions with the optimized H-bond donor and acceptor (Fig. 1c), which endows the dynamic reversible networks with exceptional shear stiffening performance (Fig. 1d). Consequently, the polytitanosiloxane (PTS) supramolecular networks exhibit a storage modulus increase of ~2800 times during the frequency range of 0.1 to 100 Hz. Furthermore, the resulting SSG exhibits minimal corrosion and low toxicity. The PTS SSG achieves a relative cell growth rate of 88.1%, which significantly surpasses 48.5% of

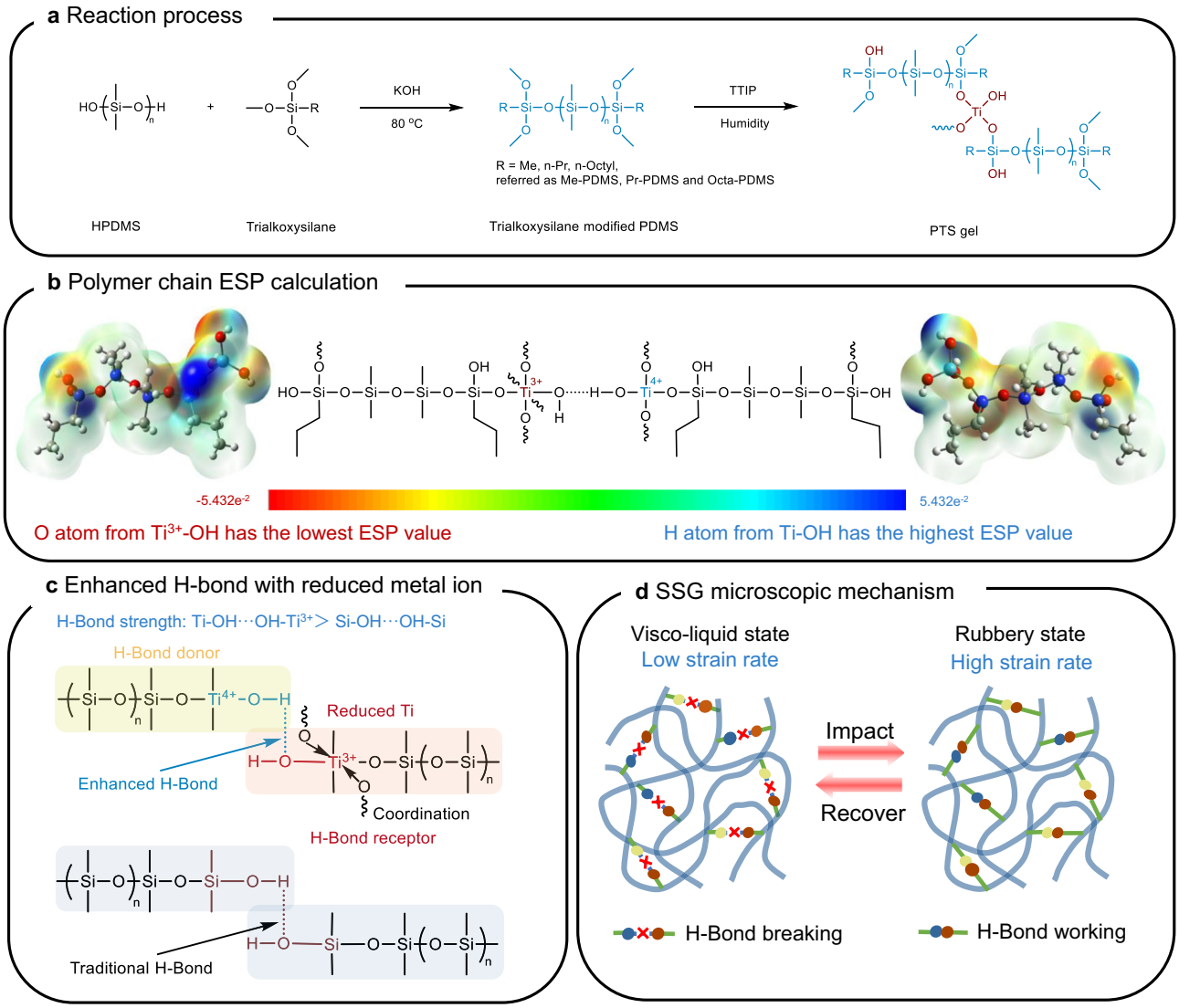

Fig. 1 | Schematic structure of the PTS SSG design. a Reaction process of PTS preparation (Me, n-Pr and n-Octyl hereinafter referred to Methyl, n-Propyl and n-Octyl groups, respectively). **b** Electrostatic potential (ESP) calculation of the two PTS polymer chains with Ti-OH and Ti^{3+}-OH group. **c** Metal ion enhanced H-bond between Ti-OH and Ti^{3+}-OH groups and traditional H-bond between silanol groups. **d** Schematic illustration of the SSG microscopic mechanism based on H-bond dynamic reversible networks.

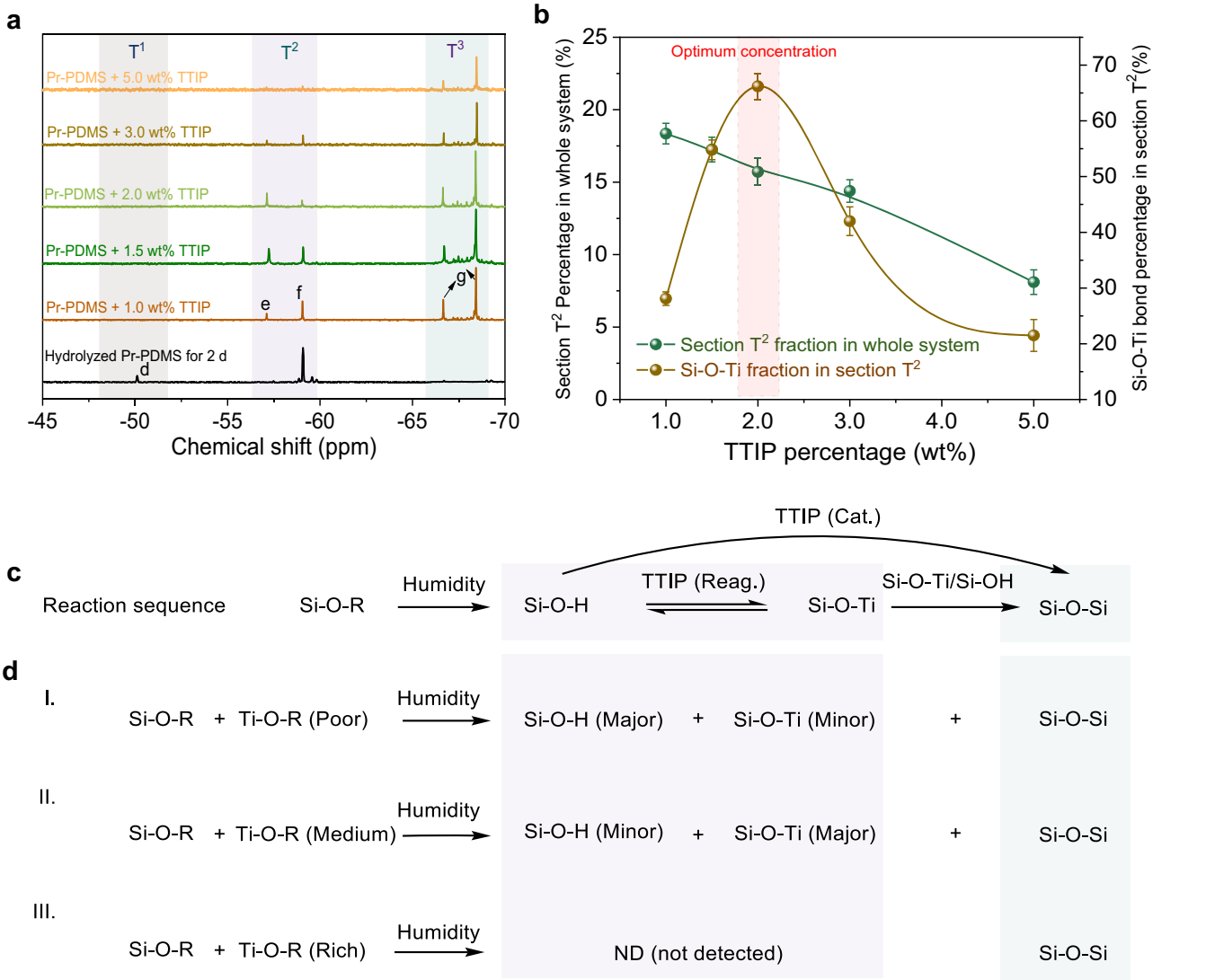

Fig. 2 | Investigation for the chemical structure of the PTS gel. a The ^{29}Si NMR spectra of the Pr-PDMS gels with different fractions of TTIP ($CDCl_3$ as testing solvent, 600 MHz magnet frequency). **b** Section T^2 percentage in the whole system and Si-O-Ti unit percentage in section T^2, $n = 5$, gel samples, data are mean ± SD. **c** Proposed reaction sequence (cat. and reag. represent catalyst and reagent in reaction) and **d** product priority with different concentrations of TTIP.

the PBS SSG. We also demonstrate its promising applications in anti-impact protection materials and flexible device sensors.

Results

Synthesis and optimization of the PTS dynamic reversible networks

To obtain a dynamic reversible network with Si-O-Ti heterostructures, we first designed and synthesized a range of siloxane-modified PDMS, followed by a heterocondensation reaction with TTIP (Fig. 1a). At the initial step, we carried out condensation reactions of Si-OH-terminated polysiloxane with three types of trimethoxysilanes of different carbon chain lengths (methyltrimethoxysilane, n-propyltrimethoxysilane, and n-octyltrimethoxysilane) and tetramethoxysilane. The modified PDMS was characterized by ^{1}H NMR and referred to as Me-PDMS, Pr-PDMS Octa-PDMS and Tri-PDMS, respectively (Supplementary Fig. 1). We evaluated the modification yields at the ends of the PDMS chains by characterizing the raw material HPDMS and the modified products using ^{29}Si NMR (Supplementary Fig. 2). The peak at −10.56 ppm chemical shift in the spectrum of HPDMS corresponded to the Si-OH terminated group, and the modification reaction yield could be determined by analyzing the proportion of the corresponding peak intensity reduction in the spectra of modified PDMS[29]. In this instance, 87.3–88.9% of the Si-OH-terminated groups were modified by alkoxysilanes. Then, to determine the reactive atom ratio of Si and Ti in the following heterocondensation process, HPDMS was characterized by gel permeation chromatography (GPC) (Supplementary Fig. 3). The number-average molecular weight (M_n) was ~38640 g mol^{-1}, and the repeating unit (n) was ~552. On this basis, we calculated the TTIP addition amount, which was approximately 1.5% by weight of HPDMS (TTIP molecular weight ~ 284 g mol^{-1}), when the molar ratio of Si and Ti atoms was equivalent. Depending on the molar ratio of Si and Ti atoms, the modified PDMS chain ends can form various building units in the presence of TTIP[29–31].

Accordingly, we investigated the structural unit of the Pr-PDMS polymer chain ends following the condensation reaction with varying fractions of TTIP. The appearance of the characteristic Si-O-Ti absorption band at 930 cm^{-1} in the FTIR spectra of Pr-PDMS with various fractions of TTIP, which was absent in the spectrum of the neat Pr-PDMS, provided evidence for the formation of Si-O-Ti bonds (Supplementary Fig. 4)[32]. The Si-O-Ti bond was further clarified by ^{29}Si NMR spectroscopy, with results shown in Fig. 2a. There were signals at −50.10 ppm in section T^1 and −58.91 ppm in section T^2 assigned to (SiO)

$\underline{Si}(OCH_3)_2CH_2CH_2CH_3$ and $(SiO)_2\underline{Si}(OH)CH_2CH_2CH_3$ units, respectively[29,33,34]. By comparing the spectra of the hydrolyzed Pr-PDMS sample for 14 d without TTIP in Supplementary Fig. 5 and after the addition of TTIP in Fig. 2a, the newly emerged e peak in was ascribed to the Si-O-Ti bond with one -OCH_3 group. The -OCH_3 group can also be evidenced by the ^{1}H NMR spectra in Supplementary Fig. 1f. The peaks e and f in section T^2 were assigned to semi-crosslinking structures with two Si-O-Si units or one Si-O-Si and Si-O-Ti units, while the signals g in section T^3 between −64.5 and −69.5 ppm were assigned to three Si-O-Si cross-linking units[35]. Furthermore, the proportion of section T^2 in the whole system and the relative abundance of Si-O-Ti and Si-OH units in section T^2 was calculated through the integration of the peaks e, f and g. The results are shown in Fig. 2b. With increasing TTIP fraction, the proportion of section T^2 in the entire system decreased, indicating TTIP's role in catalyzing the formation of cross-links primarily composed of Si-O-Si units. Under this circumstance, the cross-link bonds were irreversible and could not be reformed once created. The trend of the Si-O-Ti building unit initially rose and then declined, with the Si-O-R end group converting to the Si-OH group, which subsequently formed Si-O-Ti bonds through a hetero-condensation reaction[30,36]. Consequently, the chemical structure of the final product was significantly influenced by the varying fractions of TTIP. At a TTIP fraction of 1.0 wt%, the Si-O-Ti bond fraction in the system was limited for the lack of the Ti-O-R group. In contrast, at TTIP fractions of 3.0 wt% or higher, the homocondensation reaction of Si-OH and the formation of cross-link Si-O-Si bonds dominated the system, limiting the availability of active terminal Si-OH groups for heterocondensation reactions. The overall sequence of hydrolysis and condensation reactions, as well as the final product structure with different TTIP fractions, are summarized in Fig. 2c and d.

Subsequently, the SSG performance was evaluated by investigating the appearance status and the rheological behaviors of the PTS gels with the different fractions of TTIP (Fig. 3 and Supplementary Fig. 6). As the TTIP fraction increased, the gel was gradually transformed from liquid to solid state under room temperature (Fig. 3a). Moreover, the initial storage modulus for 2.0 and 4.0 wt% TTIP samples was 4.1×10^1 and 2.3×10^4 Pa, respectively, indicating a significant enhancement in the storage modulus as the TTIP fraction increased (Fig. 3b). The relative shear stiffening performance could be calculated using Eq. (1)[35].

$$\mathrm{RST} = \frac{G'_f - G'_i}{G'_i} \times 100\% \quad (1)$$

Where G'_i and G'_f are the initial and the final storage modulus. As can be seen from Fig. 3c, the shear stiffening performance showed a rising and then falling trend, with the best performance observed at a TTIP fraction of 2.0 wt%, where the RST of SSG increased to 1.20×10^5%. By referring to Figs. 2b and 3c, it was evident that the RST value exhibited a positive correlation with the percentage of Si-O-Ti units at the polymer chain ends. The results indicated that the proportion of Ti atoms embedded in the networks was a crucial factor influencing the performance of SSG. After 30 days of air exposure, the RST value of the gel still maintained more than 95% of its initial value, demonstrating a relatively stable shear stiffening performance (Supplementary Fig. 7). Furthermore, the stress-strain relationship of the SSG samples was investigated at various shear rates ranging from 0.05 to 2 s^{-1}, which are shown in Fig. 3d and e. As the shear rate increased, the stress response increased instantaneously, exhibiting a representative shear rate dependency (Fig. 3c)[8]. For instance, at a shear rate of 0.05 s^{-1}, the SSG with 2.0 wt% TTIP had a maximum stress of only 1.28 KPa, which increased to 11.4 KPa at a shear rate of 0.5 s^{-1}. Additionally, all stress curves increased with increasing strain and ultimately reached saturation under constant shear rate excitation, and no Payne effect occurred in the 2.0 wt% TTIP sample. However, excessive TTIP addition could lead to the formation of Ti-O-Ti units through homocondensation reactions, facilitating the formation of TiO_2 nanoparticles (Supplementary Figs. 8 and 9). The aggregation of the nanoparticles will further cause instability in the inner structure of SSG[37]. Consequently, stress in the 4.0 wt% TTIP sample, while increasing with rate, did not enhance as significantly as in the 2.0 wt% TTIP sample (Fig. 3d). This instability caused stress to decline before saturation after reaching a maximum value. Overall, the result highlights the significance of the heterogeneous Si-O-Ti architecture and the fraction of titanium atoms within the supramolecular networks in shear stiffening properties. Based on this result, we further optimized the supramolecular network by modulating the chemical structure of the chain ends.

The steric hindrance effect of terminal groups has a significant impact on the condensation reaction of polymer chains, thereby influencing the chemical composition of the supramolecular networks. In this study, due to the excessive steric hindrance of i-Pr-Si-$(OMe)_3$, resulting in low end-capping yield of Si-OH of HPDMS, we selected end-capping agents with varying carbon chain lengths to investigate the influence of steric hindrance on rheological behavior (Supplementary Fig. 10). On this basis, a range of siloxanes with three different carbon chain lengths (Me-PDMS, Pr-PDMS, and Octa-PDMS) were selected to modify the polymer ends. From Fig. 4a and Supplementary Fig. 11, we could find that the Si-O-Ti units existed in all of these three PDMS polymer chains. The Si-O-Ti bond fraction showed a decreasing trend with the increase in carbon chain length. And Octa-PDMS, with the longest C atoms, had the highest fraction 14.5% among these three. The octane group sterically hindered the homocondensation reaction between siloxane groups, facilitating the heterocondensation reaction with TTIP[38–40]. Secondly, Octa-PDMS, which had a relatively strong steric hindrance effect, required more space to form reversible networks. The Si-O-Ti unit was able to create space between the siloxanes for the long alkyl group. Figure 4c, d, e and f illustrate the mechanism. Furthermore, the rheological behaviors of the Me-PDMS, Pr-PDMS, and Octa-PDMS gels were studied. In brief, all three modified PTS gels exhibited typical shear-stiffening characteristics (Supplementary Fig. 12). However, different rapid growth rates of modulus were observed. The Me-PDMS-based SSG had the highest fraction of the Si-O-Si homogenous bonding unit, which facilitated the formation of a polymer network of PDMS chains. Therefore, the initial storage modulus of Me-PDMS was 2.27×10^2 Pa, which was the highest among these three PDMS. However, the RST value of the Me-PDMS gel was only 2.40×10^4%, relatively lower than that of Pr-PDMS and Octa-PDMS samples, likely due to its lowest fraction (9.5%) of Si-O-Ti units. In contrast, Octa-PDMS gel exhibited shear-stiffening performance with an RST value of 2.8×10^5%, compared to the other two PDMS samples, due to its highest Si-O-Ti fraction (14.5%). After comprehensive consideration of the initial modulus and SSG performance, we selected the Pr-PDMS gel as the reference subsequently. Meanwhile, it can also be concluded that the incorporated Ti atom or its surrounding chemical group in the networks was the key factor responsible for the shearing stiffening performance.

The cross-link density of the PTS gel networks was also an important factor influencing SSG performance. It was highly dependent on the number of active functional groups (Si-OR) in the polymer chain. Accordingly, HPDMS (monofunctional macromolecule), Pr-PHMS (bifunctional macromolecule) and Tri-PDMS (trifunctional macromolecule), these kinds of modified polymer chains were selected to investigate the cross-link density effect on the shear stiffening performance (Fig. 4b and Supplementary Fig. 13). As can be seen from Fig. 4b, the storage modulus of Tri-PDMS gel reached 5.54×10^4 Pa, the highest storage modulus among these three PTS gels, likely due to the formation of cross-link units at chain ends (Supplementary Fig. 14). However, the storage modulus remained stable from 0.1 to 100 Hz, exhibiting no obvious shear stiffening performance. The result was attributed to the high cross-link unit's formation without dynamic

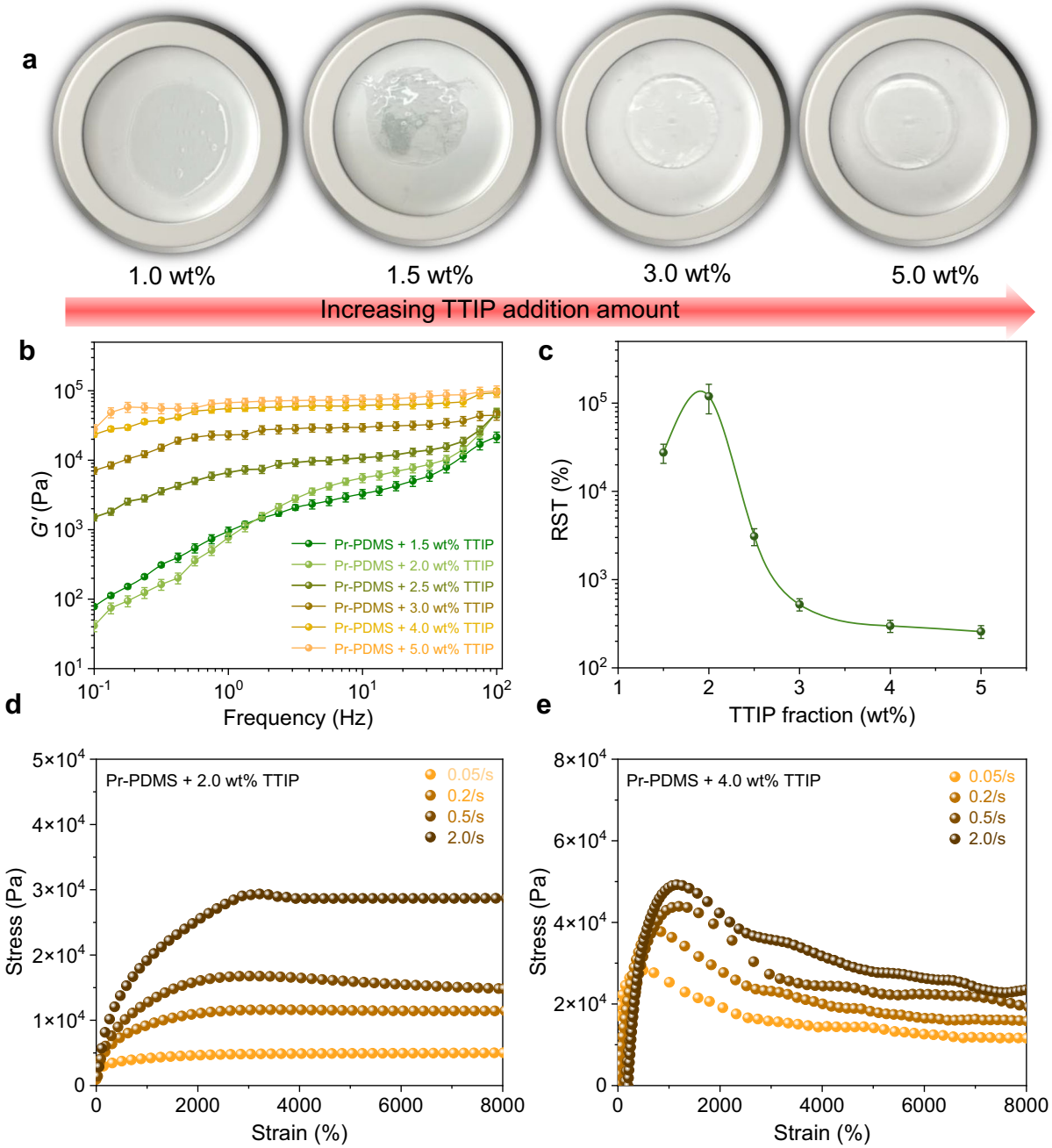

Fig. 3 | Investigation of the rheological behaviors of the PTS gel. a Optical images **b** storage modulus, $n = 5$, gel samples, data are mean ± SD and **c** RST of the PTS gels with different fractions of TTIP, $n = 5$, gel samples, data are mean ± SD. Stress-strain curves of the PTS gels with **d** 2.0 wt% TTIP and **e** with 4.0 wt% TTIP.

reversible interactions. Unlike the hydrogen bond network constructed by Ti-OH in Pr-PDMS gel (Supplementary Fig. 15), no Ti-O-H group was detected in the HPDMS gel with the same fraction of TTIP, although the Ti atoms were embedded into the supramolecular networks through the Si-O-Ti bonding (Supplementary Fig. 16 and 17).

Compared with the Pr-PDMS gel, the slight shear stiffening performance of HPDMS gel was likely a reflection of H-bond interactions between Si-OH end groups. Homogeneous H-bond networks were built, increasing the friction of polymer chains[40,41]. A more obvious increasing trend of modulus was observed in the neat Pr-PDMS sample. After hydrolyzing for 2 d, the neat Pr-PDMS sample initially exhibited a very low modulus due to the lack of crosslinked Si-O-Si structural units. However, owing to the prevalence of a large number of hydroxyl groups (Si-OH) in the system, it could be observed that its modulus also increased significantly with the shear frequency, with an RST value of 2.4×10^4%. Compared with the HPDMS gel, it demonstrated a relatively low modulus and strong frequency dependence, suggesting that the hydrolyzed Pr-PDMS was a typical shear-thickening fluid. Unfortunately, the SSG performance of the HPDMS gel and hydrolyzed Pr-PDMS was inferior to the Pr-PDMS gel, possibly because the relative strength of H-bonding interactions was weaker than that in the PTS gel. Meanwhile, due to the difference in frequency-dependent response of HPDMS and Pr-PDMS gel, it could be inferred that a dissimilar type of H-bond existed in the system in contrast to that between the Si-OH groups.

Mechanism discussion for the shear-stiffening response

To gain a deep insight into the shear stiffening mechanism, Diisopropoxy-bisethylacetoacetatotitanate (DBEAT) was used to

https://doi.org/10.1038/s41467-025-64000-1

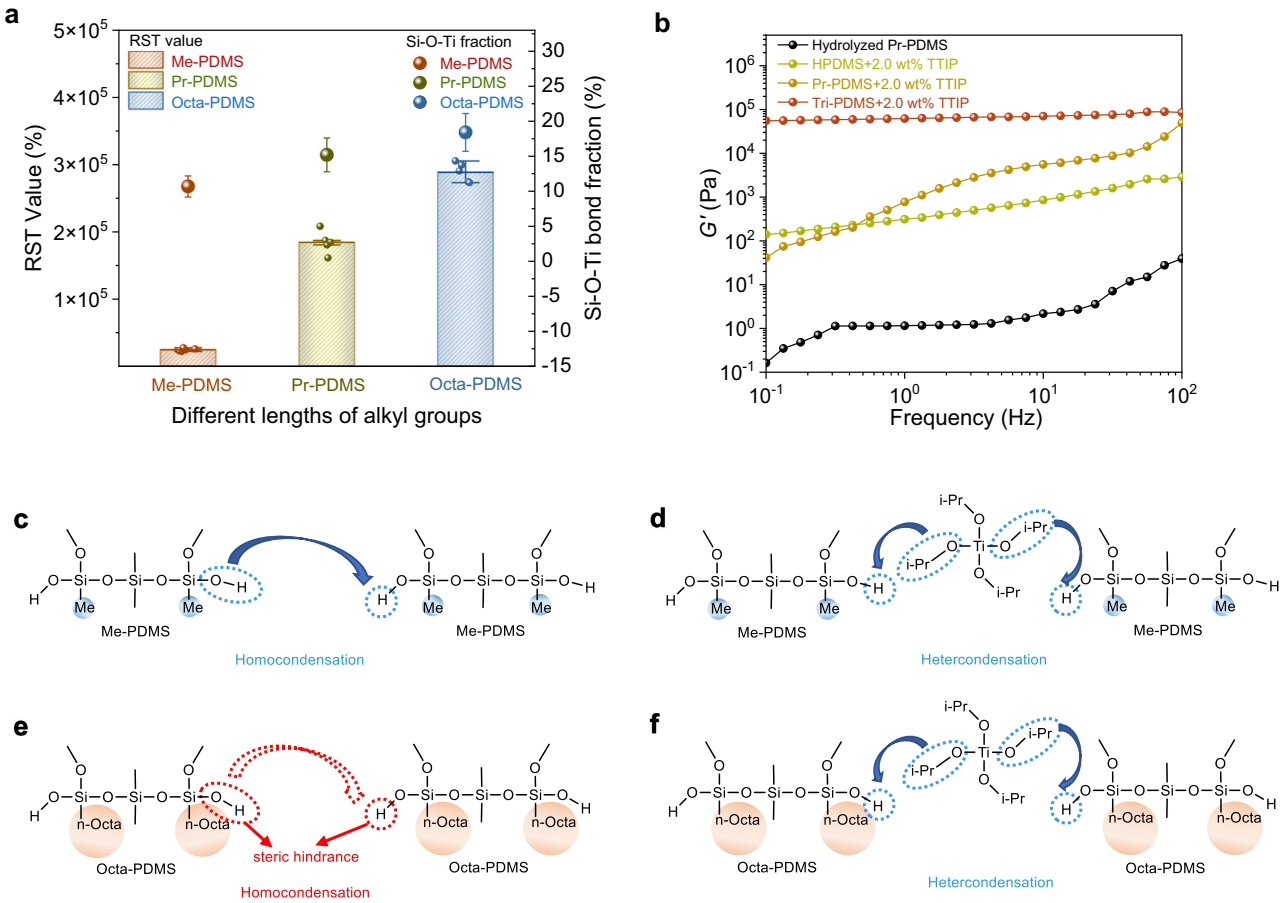

Fig. 4 | Precisely macromolecular design at the polymer ends. The storage modulus and Si-O-Ti fraction of **a** Different lengths of alkyl groups of bifunctional PDMS (Me-PDMS, Pr-PDMS and Octa-PDMS) with 2.0 wt% TTIP ($n = 5$, gel samples, values are expressed as mean ± SD). **b** Hydrolyzed Pr-PDMS sample and different number functional groups of the PTS gels (HPDMS, Pr-PDMS and Tri-PDMS) with 2.0 wt% TTIP **c** Proposed homocondensation and **d** heterocondensation reaction mechanism of the Me-PDMS **e** Proposed homocondensation and **f** heterocondensation reaction mechanism of the Octa-PDMS.

vulcanize the Pr-PDMS sample as a comparative reference with TTIP. In contrast to TTIP, DBEAT features only two chelating ligands, providing structural stability[42]. On this basis, in the DBEAT catalyst system, more Ti atoms were incorporated into the networks compared to TTIP (Fig. 5a and Supplementary Fig. 18). However, the shear stiffening performance of the gel catalyzed by DBEAT was not as effective as that catalyzed by TTIP (Supplementary Fig. 19). By comparing the shear stiffening performance of the gels catalyzed by two Ti couple agents, it could be concluded that the shear stiffening performance was not directly derived from the Si-O-Ti covalent bonds. Subsequently, to delve into the electronic states of Ti atoms, a comprehensive EPR spectra analysis was conducted. As seen in Fig. 5b, neat TTIP showed no signals in spectra, indicating that Ti existed in the form of Ti^{4+} within TTIP without any O vacancy or Ti^{3+}/Ti^{2+} defects. In contrast, DBEAT generated a signal at g = 1.99, attributed to Ti^{3+}(Supplementary Fig. 20)[43–45]. Because DBEAT is prone to forming internal coordination with the carbonyl group and Ti, the Ti d orbital overlaps with the p orbital of O in the carbonyl group[42]. The carbonyl oxygen could transfer electrons to the titanium center, resulting in a reduction of the oxidation state of Ti. In the Pr-PDMS + TTIP system, the hydrolysis of TTIP induces a pronounced redshift of the UV-Vis absorption band beyond 330 nm, indicative of Si–O–Ti cluster formation. This redshift arises from oxygen-to-metal charge transfer ($O \rightarrow Ti^{4+}$) interactions within the Si–O–Ti network, which further trigger partial reduction of Ti^{4+} to Ti^{3+}, as evidenced by extended absorption features in the visible region (Supplementary Fig. 21 and 22)[46–50]. To further verify this point, we studied the molecular orbital information of TTIP, HPDMS and PTS chains. As illustrated in Fig. 5c, the LUMO of the Si-O-Ti(OH) polymer chain ends was located at the Ti (d) orbit. It was observed that the orbital was relatively lower compared with the LUMO of in pristine TTIP and the Pr-PDMS chain. The result indicated that the partial Ti^{4+} could be reduced to Ti^{3+}.

To further emphasize the crucial role of Ti-OH group H-bond and the metal ion mediation strategy, we analyzed the molecular orbital information of Ti as well as the chemical environment around the Ti atoms. First, electrostatic potential (ESP) was used to analyze the atomic charge distribution of the polymer chain ends. Notably, the H atom from the Ti-OH end group stood out with the highest electrostatic potential within the entire polymer chain (Supplementary Fig. 23). In contrast, the O atom from Ti^{3+}-OH end groups was prominent for the lowest electrostatic potential. On this basis, the enhanced H-bond could be built between the Ti-OH and Ti^{3+}-OH groups. To further clarify the H-bond between the polymer chains, ^1H NMR spectroscopy was utilized to investigate the changes in peak intensity and chemical shift of the Si-OH and Ti-OH groups. We also observed that peak b, assigned to the Si-OH group, shifted lowfield from 1.61 to 1.72 ppm in the PTS gel (Fig. 5d and Supplementary Fig. 24)[51]. The results suggested the existence of H-bonding between the hydroxyl groups[52–54]. More importantly, from Fig. 5e and Supplementary Fig. 25, we also observed four peaks around 2.30 ppm, which were assigned to the Ti-OH group[55]. The peaks from lowfield to high-field represented free Ti-OH, H-bonded Ti-OH, H-bonded Ti^{3+}-OH and free Ti^{3+}-OH, respectively. The result not only confirmed the presence of Ti^{3+}-OH, but also provided evidence for the H-bond between the

https://doi.org/10.1038/s41467-025-64000-1

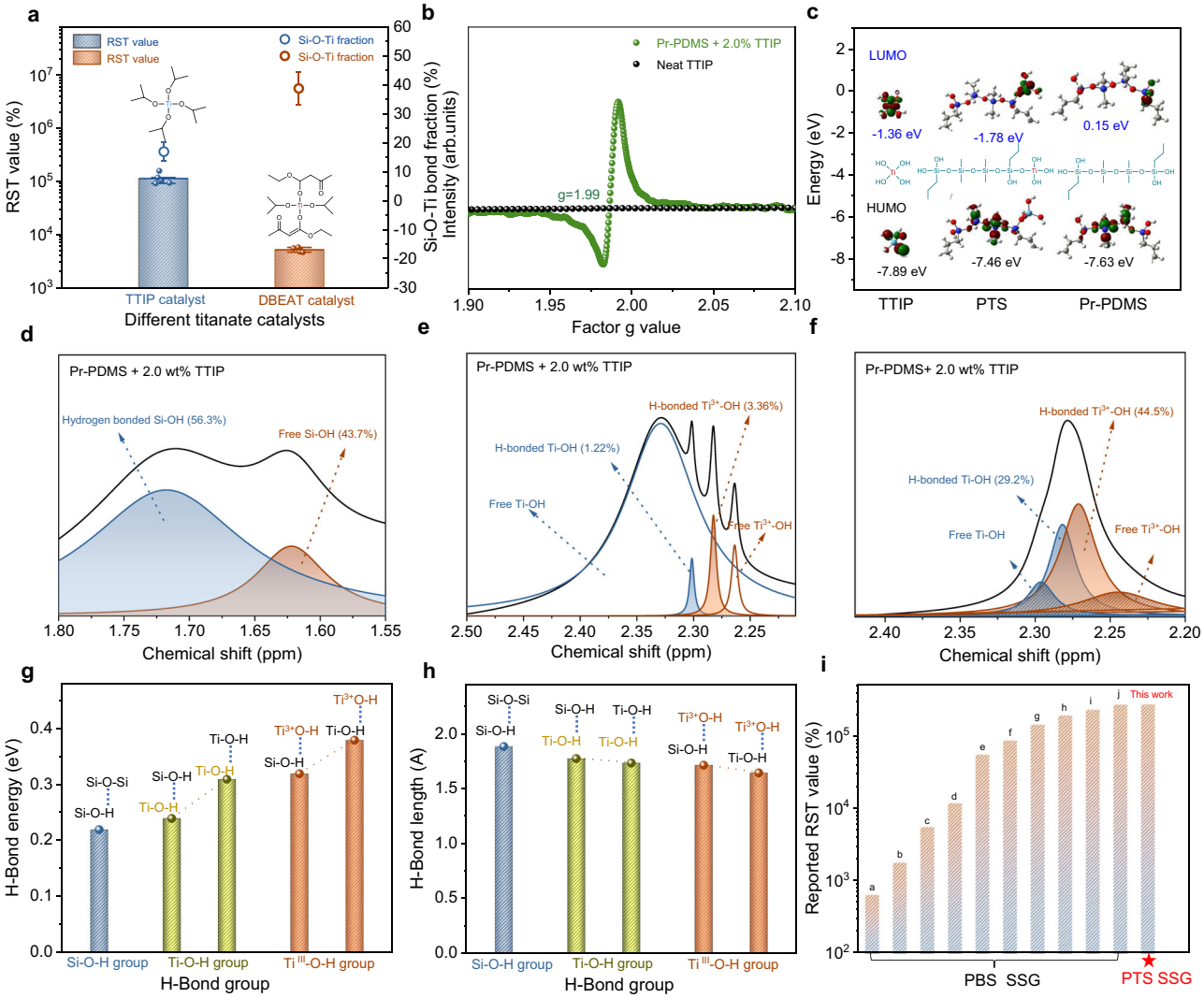

Fig. 5 | Identification and mechanism investigation of the H-bond between the polymer chains. a The Si-O-Ti fractions and SSG RST of the Pr-PDMS with equal ratios of TTIP and DBEAT (Bars represent RST values and solid balls are expressed as individual tests, while hollow circles represent Si-O-Ti bond fraction, n = 5, gel samples, values are expressed as mean ± SD). **b** EPR spectra of the PTS gel. **c** The LUMO and HOMO of the TTIP, PTS chain and Pr-PDMS chain. ^{1}HNMR spectra of the PTS gel with 2.0 wt% fractions of TTIP in the range of **d** 1.80–1.55 ppm, **e** 2.50–2.20 ppm after 12 h, **f** 2.50–2.20 ppm after 48 h ($CDCl_3$ as testing solvent, 400 MHz magnet frequency). **g** H-bond energy and **h** bond length of the hydroxyl groups. **i** SSG performance comparison with the reported value of PBS SSG (a–j refer to previously reported works respectively[5–8,35,65–69]).

Ti-OH groups. The H-bonding effect strengthened as the reaction duration extended. Therefore, after 48 h, the concentration of Ti^{3+} ions and the hydrogen-bonded hydroxyl groups in the system increased significantly (Fig. 5f and Supplementary Fig. 26).

Then, we evaluated the H-bond strength through computational methods (Supplementary Fig. 27). As shown in Fig. 5g and h, the conventional Si-OH groups had relatively weaker H-bond energy with 0.22 eV and 1.89 Å length. When a silicon hydroxyl group is replaced by a titanium hydroxyl group, the hydrogen bond energy increases by only 0.02 eV. The energy enhancement of ~0.09 eV was more obvious when both the H-bond donor and acceptor were replaced by Ti-OH. When the oxidation state of Ti was changed, the electron cloud distribution of the O element in the hydroxyl group would also change accordingly, which can affect the hydrogen bond energy. Therefore, in contrast to Ti^{4+}, the accumulation of electrons on Ti^{3+} led to an increase in negative charge around the O atom of Ti-OH. As a result, the intermolecular H-bond became stronger, with an increase in bond energy (0.38 eV vs. 0.31 eV) and a decrease in bond length (1.65 Å vs. 1.78 Å). Due to the relatively stronger H-bond strength of Ti^{3+}-OH groups as the acceptor, we found that the PTS gel with 2 wt% TTIP had the highest proportion of hydrogen-bonded Ti^{3+}-OH groups, resulting in the best SSG performance, which was consistent with the results above. The results confirmed that the metal ion mediation strategy was capable of regulating the charge distribution of both the donor and the receptor simultaneously, thereby enhancing the strength of the H-bond. Consequently, the PTS gel exhibited an exceptional shear stiffening performance compared with the current PBS SSG (Fig. 5i).

Based on these findings, under low strain rate external forces, the H-bond has sufficient time to break, and the damping force driven by the entanglement of polymer networks becomes the main barrier to the gliding of polymer chains. Therefore, the SSG exhibited viscous characteristics with flowability at a macroscale level. However, it is important to note that H-bond is more transient, dynamically variable and vulnerable than covalent bonds (e.g., Si-O-Si bond). When subjected to high rates of external stress, the dynamic reversible network constructed by the H-bond becomes resistant to breaking. In addition, the disordered polymer chains do not have enough time to relax and disassemble, hindering their movement. The mechanical properties of the SSG are predominantly influenced by the rotation of chain

https://doi.org/10.1038/s41467-025-64000-1

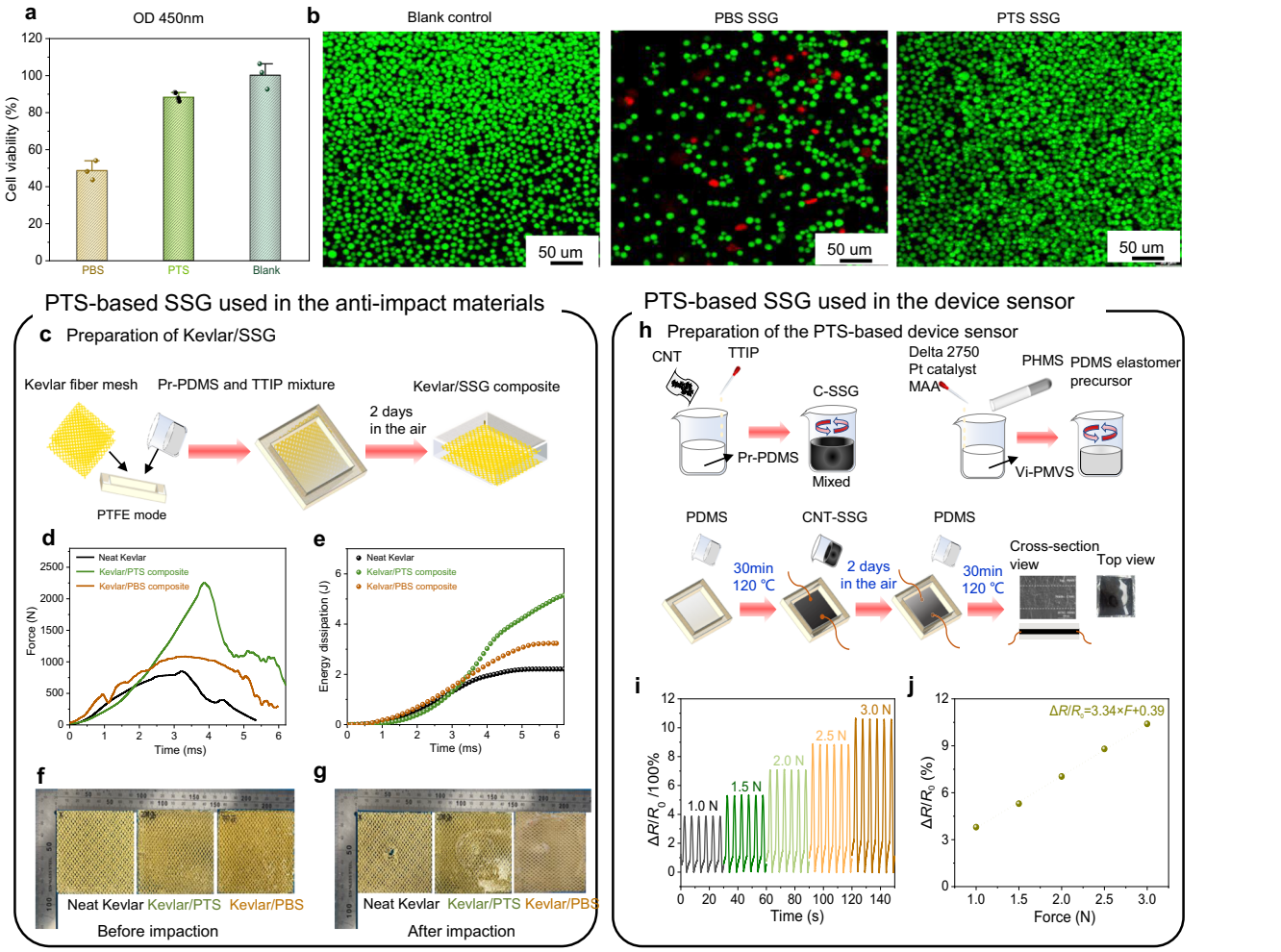

Fig. 6 | Cytotoxicity assessment and practical applications of the PTS SSG. **a** CCK8 cell metabolism assay of the blank control group, PBS gel and PTS gel after culturing 48 h (n = 3, biological replicates, values are expressed as mean ± SD). **b** The staining images of live and dead cells of Caco-2 cells after co-culture with blank control, PBS and gel PTS gel (green spheres: live cells, red spheres: dead cells, scale bar 50 μm). **c** The schematic illustration of the fabrication process of the Kevlar/SSG composite. **d** The force-time curves and **e** the energy dissipation of the neat Kevlar and Kevlar/SSG composite. **f**, **g** Optical images of the neat Kevlar and Kevlar/SSG composite before and after impaction, respectively. **h** The schematic illustration of the fabrication process of the flexible device. **i** The relationship between the resistance changes and the applied forces of the PDMS/c-STG/PDMS sandwich device under various external forces. **j** Experimental data and fitting curve of ΔR/R0 versus force.

segments, resulting in a high stiffness state at the macroscale. The entire process is illustrated in Fig. 1d.

Corrosion and cytotoxicity properties and application of the PTS

Studying the SSG's corrosivity issue with metal is important for evaluating its safety during its practical production and processing. Therefore, to evaluate the corrosivity of the PTS gel, we directly placed the samples of BA, PBS, TTIP, and PTS in direct contact with 304 stainless steel pieces and placed them in an oven at 160 °C for two days to observe and compare the morphological changes on the contact surface of the stainless steel. It can be seen from Supplementary Fig. 28 that due to the strong corrosivity of BA at high temperatures, there is a significant darkening in color on the contact surface with the steel, indicating that some reaction has occurred between BA and the substances in stainless steel, resulting in a corrosion reaction. Meanwhile, the phenomenon was also observed on the surface of the steel alloy in contact with the PBS gel. In contrast, after 2 days of high-temperature contact, there were no significant changes in the surfaces of the alloy steel in contact with TTIP and PTS gel compared to the blank group, indicating that TTIP and PTS gel exhibited negligible corrosion behavior. This result indicated that the PTS-based SSG option can effectively avoid the corrosion of PBS SSG, thereby avoiding the safety problems of PBS during production and processing.

More importantly, the cytotoxicity of the PTS gel to Caco-2 cells was investigated to evaluate the toxicity to human beings. The viability of Caco-2 cells in PBS, PTS and control groups was tested through the CCK8 assay. As shown in Fig. 6a, the relative growth rate (RGR) was calculated by OD values at 450 nm. The RGR of PBS and PTS gel was 48.5% and 88.1%, respectively. We found that PBS has a significant inhibitory effect on Caco-2 cell growth (Grade 3, 25–49%, severely poisonous). In contrast, the PTS gel was slightly poisonous (Grade 1, 75–99%, slightly poisonous). The result suggested that the PTS gel significantly reduced the toxicity to human intestinal cells and could be a safe alternative to PBS. Meanwhile, the live-dead cell staining images also proved that the PTS gel had obvious advantages over the PBS gel in the cell co-growth environment, because the attached cells did not exhibit any changes in their morphology when compared to the control group (Fig. 6b).

Given the reversible soft-rigid mechanical transformation behavior, SSG exhibits great potential for damping and shock energy dissipation[56]. Accordingly, a Kevlar/SSG composite was developed to investigate the impact resistance and energy dissipation capabilities of the SSG. The preparation process of the composite is detailed in Fig. 6c. The anti-impact performance of the composite fabrics was

evaluated using a drop hammer test. During the penetration process, the relationship between acceleration and time was recorded, and energy-time curves were derived through mathematical integration (Fig. 6d, e). In comparison to the peak force of pure Kevlar, which was 8.5×10^2 N, the maximum force of the Kevlar/SSG composite increased significantly to 1.4×10^3 N.

The SSG initially encountered an external force, at which point it dissipated a portion of its energy to mitigate the velocity of the fall and subsequently reduce the force acting on the substrate. Consequently, the shear rate increased, leading to rapid movement of the polymer chains. A large number of Ti-O-H terminated groups engaged in H-bonding interactions, effectively countering substrate deformation, and resulting in a substantial surge in the storage modulus. Compared to pure Kevlar fibers and Kevlar/PBS composite, the Kevlar/PTS composite dissipated approximately 1.35×10^2 and 6.07×10^1% more energy. Visual inspection from Fig. 6f and g revealed that while the fibers of neat Kevlar were pulled out and even torn after impact, the Kevlar/SSG composite showed no signs of fracture or disconnection. The SSG's impact on the failure mode and increased impact force indicated its ability to enhance slipping resistance and limit the relative movement of the Kevlar fibers, thereby distributing more fibers under impact. This demonstrated that SSG not only absorbed energy from high-velocity impacts but also protected the substrate from severe damage.

Owing to its exceptional flexibility and non-toxic nature, the as-prepared SSG was further explored for its potential as a flexible substrate for conductive nanomaterials (Supplementary Fig. 29). In this context, CNTs were introduced as a nanofiller for conductive modification in the SSG. Firstly, the electrical conductivity of the SSG-based composite was investigated. Notably, the composite's resistivity exhibited a significant decrease when the CNT weight fraction was less than 3.5%. It then gradually decreased to 2.1×10^1 Ω·m and remained stable until saturation, indicating conductive percolation (Supplementary Fig. 30a)[57–59]. Importantly, the introduction of CNTs did not compromise the shear-stiffening performance of the SSG, with an RST of 6.0×10^4%, comparable to pure SSG (Supplementary Fig. 30b). Leveraging its composite's flexibility and conductivity, an SSG mixture with 3.0 wt% CNTs and 2.0 wt% TTIP was employed to construct an electroactive layer for a sandwich sensor device. The electroactive layer was encapsulated by two PDMS-based insulating layers, providing both flexibility and mechanical robustness to the sensor (Fig. 6h). The as-prepared flexible sensor was subjected to varying external forces simulated by a dynamic mechanical analyzer (DMA) at room temperature. The resistance was monitored using a universal meter under dynamic external forces. The change in resistance was characterized using Eq. (2)

$$\frac{\Delta R}{R_0} = \frac{R - R_0}{R_0} \times 100\% \tag{2}$$

to define the relative resistance change ratio to characterize the mechano-electrical properties. Under external stimuli, the sensor's resistance, derived from the SSG/CNT composite, increased and decreased periodically at a fixed frequency due to the intermittent breakage and recovery of the conductive network (Fig. 6i)[60]. Notably, the peak value of $\Delta R/R_0$ augmented with increasing forces within the 1.0 to 3.0 N range. The device exhibited exceptional sensitivity and consistent signal output in response to stimuli throughout bending-releasing cycles. Furthermore, the sensor's $\Delta R/R_0$ exhibited nearly linear responsiveness in bending experiments, indicating the mechano-electric stability of the SSG-based sensor.

Discussion

We demonstrated a key strategy to achieve a high shear stiffening performance in supramolecular gels by metal-ion mediated H-bond enhancement strategy. A PTS-based SSG is designed as a concept example in which multivalent titanium ions were introduced into the dynamic reversible network. By regulating the electrostatic potential of both H-bond donors and acceptors by Ti^{4+} and Ti^{3+} ions, a supramolecular network with enhanced H-bond was successfully constructed, obtaining a shear stiffening response of ~2800 times. Moreover, the resulting PTS SSG exhibited negligible corrosiveness and cytotoxicity. These intriguing features collectively make the PTS gel a promising candidate for a safe and non-toxic SSG. Additionally, we demonstrated its potential application in impact protectors and flexible device sensors, which also have broad prospects. We believe that the strategy of metal-ion-mediated design can be easily extended to other dynamic reversible network constructions, opening up avenues for developing smart materials with desirable properties.

Methods

Materials

α,ω-Hydroxyl-terminated polydimethylsiloxane (HPDMS, RTV 107 silicon oil) was provided by Hubei Xingfa Chemicals Group Co., Ltd. Methyltrimethoxysilane, propyltrimethoxysilane, octyltrimethoxysilane, tetramethoxysilane, potassium hydroxide (KOH), titanium tetraisopropanolate (TTIP) and BA were purchased from Aladdin Chemical Reagent Co., Ltd. Diisopropoxy-bisethylacetoacetatotitanate (DBEAT) was provided by Shanghai Macklin Biochemical Technology Co., Ltd. Vinyl MQ silicone resin (DT-2750) was provided by Guangzhou Delta Organic Silicon Technology Development Co., Ltd. Vinyl silicon oil (Vi-PDMS, DY-V401, CP: 20000 mpa. s) was purchased from Shandong Dayi Chemical Co., Ltd. Hydrogen polydimethylsiloxane (PHMS, RH-LHC-3) was purchased from Zhejiang Runhe Organic Silicon New Materials Co., Ltd. Karstedt's catalyst (Platinum (0)-1,3-divinyl-1,1,3,3-tetramethyldisiloxane diluent solution) was provided by Shanghai Bozhijie New Materials Co., Ltd. Reaction inhibitor (1-ethynyl-1-cyclohexanol) was purchased from Wuhan Chengtian Fine Chemical Co., Ltd. Carbon nanotube (CNT, Matrix 611) was provided by Okoh Ail Trade (Shenzhen) Co., Ltd. Kevlar fiber mesh was purchased from Dongguan Sovit Special Line Band Co., Ltd. For the cytotoxicity test, fetal bovine serum (FBS, SA311) was purchased from Sai'ao Mei Cell Technology (Beijing) Co., Ltd. Phosphate Buffer Solution (PBS, P1020) was purchased from Beijing Solarbio Science & Technology Co., Ltd. Cell-counting-kit-8 (CCK8, HC0854) was provided by WILBER. Penicillin, streptomycin (Product No.60162ES76), and live cell/dead cell double staining kit were purchased from Yeasen Biotechnology (Shanghai) Co., Ltd. Caco-2 cells (Product No. CL-0050) were purchased from Wuhan Pricella Biotechnology Co., Ltd. The Caco-2 cells line were authenticated using STR profiling technology by the supplier.

Synthesis of a range of siloxanes-modified polydimethylsiloxane

100 g HPDMS was added into a three-neck flask and heated in a vacuum environment at 80 °C for 1 h to remove moisture. Under a nitrogen atmosphere, 1.5 mL of 1% KOH in propyltrimethoxysilane (or in 1.27 mL and 2.20 mL of methyltrimethoxysilane and octyltrimethoxysilane, respectively) solution was added to the flask at 80 °C for 1 h. Subsequently, 100 µL octanoic acid was added to the mixture and stirred continuously for another 1 h to neutralize the excess KOH in the system. Finally, the methyltrimethoxysilane, propyltrimethoxysilane, octyltrimethoxysilane, and tetramethoxysilane-modified PDMS were obtained by connecting the flask to a vacuum pump at 120 °C to remove unreacted reactants and recorded as Me-PDMS, Pr-PDMS, Octa-PDMS, and Tri-PDMS, respectively.

Preparation of PTS SSG

In brief, 10 g of Me-PDMS, Pr-PDMS, Octa-PDMS and Tri-PDMS, and 0.20 g of TTIP were charged into a flask and stirred under nitrogen for 20 min. After that, the mixture was poured into a polypropylene mold and vulcanized in the air under natural environment conditions (25 °C and 50% humidity) for 48 h. To evaluate the Ti-O-H H-bonding effect

on SSG behaviors, 10 g Pr-PDMS was vulcanized by 0.30 g DBEAT (equal Si/Ti molar ratio with TTIP) in the same condition as TTIP.

Preparation of PBS SSG

According to the previously reported contribution of PBS SSG, BA was mixed with HPDMS and stirred at room temperature until homogeneous. Then the mixture was heated at 180 °C for 2 h and was stirred every 20 min to keep the reaction adequate. The PBS SSG was obtained after the mixture was cooled down to room temperature.

Preparation of PDMS/C-SSG/PDMS sandwich device

PDMS encapsulated layer: 50 g DT-2750, 50 g Vi-PDMS, 3.63 g PHMS, 0.25 g Pt Karstedt's catalyst and 0.015 g 1-ethynyl-1-cyclohexanol were mixed under mechanical stirring for 30 min at room temperature. Then the encapsulated layers were prepared by pouring the mixed precursor into a PTFE mode in an oven at 90 °C for 120 min for vulcanization. C-SSG electroactive layer: 50 g Pr-PDMS, 1 g TTIP and 1.5 g CNT were mixed for 30 min and then under ultrasonic treatment at room temperature. The C-SSG layer was obtained by pouring the mixture onto the PDMS layer and keeping it in the air for 48 H. The sandwich device was constructed by sequentially preparing C-SSG, PDMS layer on the bottom PDMS layer.

Preparation of Kevlar fiber mesh-reinforced SSG composite

Kevlar fiber mesh was cut into squares of 100 × 100 mm size and then put into a polytetrafluoroethylene mold. In the impact test, two layers of Kevlar fiber mesh were used. Then the SSG/Kevlar composite was obtained by pouring the Pr-PDMS and TTIP mixture (TTIP weight fraction is 2.0 %) into the mold and keeping it in the air for 48 H at room temperature for vulcanization.

Materials characterization

The Infrared measurements of the Pr-PDMS SSG with different concentrations of TTIP were performed by an FTIR spectrometer (Thermo Scientific Nicolet 6700) in ATR mode. The ^{1}H NMR spectra were obtained on a spectrometer (AVANCE III 400 MHz). The ^{29}Si NMR spectra were acquired using a spectrometer (AVANCE III HD, 600 MHz) equipped with CryoProbe BBFO, operating at 119.22 MHz for ^{29}Si NMR measurements. The 200 µL sample and 4 mg shiftless relaxation reagents $Cr(acac)_3$ were added to 400 µL $CDCl_3$ containing tetramethylsilane (TMS) as an external reference. All the spectra were recorded at 298 K. The ^{29}Si NMR spectra were measured using the spectra width of 23809 Hz, inverse gated decoupling was applied during acquisition (0.344 s) with 2 s relaxation delay time. The software topspin 3.2 was used for data collection. For NMR spectra analysis, the software MestReNova 14.0 was used in this study. The rheological behaviors of all test samples were examined using a rheometer (Haake Mars40) with the shear frequency increasing from 0.1 to 100 Hz, and then strain amplitude was set at 1% under room temperature. Under the condition of static shear tests, according to strain rate = strain/time, and by changing the sampling time of the rheometer, we could obtain the stress–strain curves under the excitation of different rates. The software Rheowin 4.91 was used to collect data. A gel permeation chromatogram of HPDMS was recorded in chloroform at a flow rate of 1 mL/min as a mobile phase. Monodisperse PDMS standards were used to normalize the instrument. The resistivity of C-SSG with different concentrations of CNT was measured by a digital four-probe tester (Suzhou Jingge, M-3 mini type). Each testing sample was made into a cylinder with 50 mm diameter and 6 mm height. The BA, TTIP, PBS gel, and PTS gel samples were placed directly onto 304 stainless steel pieces in 25 × 50 mm size in a 160 °C oven for 2 days to test the metal corrosivity test.

Cytotoxicity experiments

The relative growth rate and toxicity of cells were determined by CCK8 assay. The PBS and PTS gels were coated onto cell slides and then under ultraviolet irradiation for 30 min. The glass slides were placed in 24-well plates with Caco-2 cells, which were cultured in DMEM culture medium containing 20% FBS and 1% streptomycin–penicillin and maintained under a 5% CO_2 atmosphere at 37 °C. Caco-2 cells in the logarithmic growth phase were harvested and adjusted to an appropriate concentration before being seeded onto gels-coated coverslips in a 24-well plate at a density of 15,000 cells per well. Following 48 h of culture, the culture medium was aspirated and the cells were gently washed once with PBS. Subsequently, the cells were detached by trypsinization (3 min digestion), collected by centrifugation, and resuspended in 300 µL of complete medium. For viability assessment, 100 µL aliquots of the cell suspension were transferred to a 96-well plate, mixed with 10 µL of CCK-8 reagent, and incubated for 2 h at 37 °C in a 5% CO_2 atmosphere. Absorbance at 450 nm was then measured using a microplate reader (Tecan Infinite 200pro), with each experimental condition assayed in triplicate. The relative growth rate (RGR) could be calculated by the following Eq. (3):

$$RGR = \frac{OD_1}{OD_0} \times 100\% \tag{3}$$

where OD_1 and OD_0 represented OD values of the experimental group and control group, respectively.

For capturing live/dead cell staining images, following 3-minute trypsin digestion and centrifugation, the cell pellet was resuspended in 500 µL PBS containing 0.1% Calcein-AM and 0.3% propidium iodide (PI). The cell suspension was then transferred to a fresh 24-well plate and incubated for 15 min at 37 °C under 5% CO_2 atmosphere. Cell viability was assessed using confocal laser scanning microscopy (10× objective), with image acquisition performed at excitation wavelengths of 490 nm (for Calcein-AM, live cells) and 545 nm (for PI, dead cells).

Drop hammer tests

The anti-impact performance of the composite mesh was tested by a drop hammer. The force-time relationship was recorded during the penetration by a drop hammer impact tester (Instron-9350). A total of 2.5 kg loading dropped freely from the height of 500 mm. The acceleration sensor was set on the impact head, and the oscilloscope recorded the change in the acceleration during the puncture process. The software CeastVIEW6.43 was used to collect data.

Electric signal tests of the sandwich device sensor

In the force sensor experiment, the externally applied force between 1.0 and 3.0 newton at 0.2 Hz frequency was supplied by a dynamic mechanical analyzer (DMA 8000, Perkin Elmer) in auto-tension mode. The resistance of the device was accorded by a universal meter (Keithley 6517B) under different applied forces.

Computational methods

The calculations were performed using the Vienna ab initio simulation package code (VASP)[61]. The wave function was expanded by the plane wave, with a kinetic cut-off of 520 eV. The generalized gradient approximation with the spin-polarized Perdew–Burke–Ernzerhof (PBE) functional was used. A Monkhorst–Pack grid of (2 × 2 × 2) k-points was used[62]. A 3D-periodic cubic unit cell of 30 × 30 × 30 Å was used for simulations. The molecular orbital calculations with the hybrid functional calculations(B3LYP) were performed with Gaussian 16 according to previous studies, with a 6–311 + + G(d,p) basis set[63]. The intermolecular bond energy between molecules A and B was computed as:

$$E_{inter} = E_A + E_B - E_{total} \tag{4}$$

Reporting summary

Further information on research design is available in the Nature Portfolio Reporting Summary linked to this article.

Data availability

The data that support the findings of this study are available in figshare with the identifier https://doi.org/10.6084/m9.figshare.29625734[64]. All data are available from the corresponding author upon request. Source data are provided with this paper.

References

1. Zhao, Y. et al. Elasticity-controlled jamming criticality in soft composite solids. *Nat. Commun.* **15**, 1691 (2024).
2. Qiao, H., Wu, B., Sun, S. & Wu, P. Entropy-driven design of highly impact-stiffening supramolecular polymer networks with salt-bridge hydrogen bonds. *J. Am. Chem. Soc.* **146**, 7533–7542 (2024).
3. Plant, D. & Leevers, P. Injection moldable rate stiffening re-entrant cell arrays for wearable impact protection. *Polym. Eng. Sci.* **60**, 1546–1555 (2020).
4. He, Q. et al. Impact resistance of shear thickening fluid/kevlar composite treated with shear-stiffening gel. *Compos. A-Appl. S.* **106**, 82–90 (2018).
5. Qu, P., Lv, C., Qi, Y., Bai, L. & Zheng, J. A highly stretchable, self-healing elastomer with rate sensing capability based on a dynamic dual network. *ACS Appl. Mater. Interfaces* **13**, 9043–9052 (2021).
6. Wu, Q. et al. Highly stretchable and self-healing "solid–liquid" elastomer with strain-rate sensing capability. *ACS Appl. Mater. Interfaces* **11**, 19534–19540 (2019).
7. Liu, Z., Picken, S. J. & Besseling, N. A. M. Polyborosiloxanes, synthetic kinetics, and characterization. *Macromolecules* **47**, 4531–4537 (2014).
8. Wang, S. et al. Stretchable polyurethane sponge scaffold strengthened shear stiffening polymer and its enhanced safeguarding performance. *ACS Appl. Mater. Interfaces* **8**, 4946–4954 (2016).
9. Li, X. et al. Non-negligible corrosion from vaporized boric acid on 304 stainless steel. *J. Nucl. Mater.* **574**, 154188 (2023).
10. Xiao, Q. et al. The effects of temperature and aeration on the corrosion of A508III low alloy steel in boric acid solutions at 25–95 °C. *J. Nucl. Mater.* **480**, 88–99 (2016).
11. Hadrup, N., Frederiksen, M. & Sharma, A. K. Toxicity of boric acid, borax and other boron containing compounds: A review. *Regul. Toxicol. Pharmacol.* **121**, 104873 (2021).
12. Heindel, J. J., Price, C. J. & Schwetz, B. A. The developmental toxicity of boric acid in mice, rats, and rabbits. *Environ. Health Persp.* **102**, 107–112 (1994).
13. Kato, A. et al. Seawater fish use an electrogenic boric acid transporter, Slc4a11A, for boric acid excretion by the kidney. *J. Biol. Chem.* **299**, 102740 (2023).
14. Markwick, P. R. L., Sprangers, R. & Sattler, M. Dynamic effects on J-couplings across hydrogen bonds in proteins. *J. Am. Chem. Soc.* **125**, 644–645 (2003).
15. Xie, Z. et al. Dynamic-to-static switch of hydrogen bonds induces a metal–insulator transition in an organic–inorganic superlattice. *Nat. Chem.* **16**, 1803–1810 (2024).
16. Zhang, H. et al. Programming chain-growth copolymerization of DNA hairpin tiles for in-vitro hierarchical supramolecular organization. *Nat. Commun.* **10**, 1006 (2019).
17. Cheng, T. et al. Efficient electron transfer across hydrogen bond interfaces by proton-coupled and -uncoupled pathways. *Nat. Commun.* **10**, 1531 (2019).
18. Deng, Y., Zhang, Q. & Qu, D.-H. Emerging hydrogen-bond design for high-performance dynamic polymeric materials. *ACS Mater. Lett.* **5**, 480–490 (2023).
19. Song, X. et al. Design rules of hydrogen-bonded organic frameworks with high chemical and thermal stabilities. *J. Am. Chem. Soc.* **144**, 10663–10687 (2022).
20. Tian, Y. et al. Effect of ion-specific water structures at metal surfaces on hydrogen production. *Nat. Commun.* **15**, 7834 (2024).
21. Liang, Y., Dong, H., Aurbach, D. & Yao, Y. Current status and future directions of multivalent metal-ion batteries. *Nat. Energy* **5**, 646–656 (2020).
22. Schroeder, M. A., Ma, L., Pastel, G. & Xu, K. The mystery and promise of multivalent metal-ion batteries. *Curr. Opin. Electrochem.* **29**, 100819 (2021).
23. Panda, S., Dhara, S., Singh, A., Dey, S. & Kumar Lahiri, G. Metal-coordinated azoaromatics: Strategies for sequential azo-reduction, isomerization and application potential. *Coord. Chem. Rev.* **475**, 214895 (2023).
24. Wang, J.-W., Jiang, L., Huang, H.-H., Han, Z. & Ouyang, G. Rapid electron transfer via dynamic coordinative interaction boosts quantum efficiency for photocatalytic CO_2 reduction. *Nat. Commun.* **12**, 4276 (2021).
25. Abdinejad, M. et al. Eliminating redox-mediated electron transfer mechanisms on a supported molecular catalyst enables CO_2 conversion to ethanol. *Nat. Catal.* **7**, 1109–1119 (2024).
26. Kim, J. K. et al. Elucidating the role of metal ions in carbonic anhydrase catalysis. *Nat. Commun.* **11**, 4557 (2020).
27. Ding, J. et al. Zincophilic sites enriched hydrogen-bonded organic framework as multifunctional regulating interfacial layers for stable zinc metal batteries. *Angew. Chem. Inter. Ed.* **64**, e202416271 (2025).
28. Huang, X. et al. Structural basis for two metal-ion catalysis of DNA cleavage by Cas12i2. *Nat. Commun.* **11**, 5241 (2020).
29. Bayer, E., Albert, K., Reiners, J., Nieder, M. & Müller, D. Characterization of chemically modified silica gels by ^{29}Si and ^{13}C cross-polarization and magic angle spinning nuclear magnetic resonance. *J. Chromatogr. A* **264**, 197–213 (1983).
30. Hoebbel, D., Reinert, T. & Schmidt, H. 29Si and 17O NMR investigations on Si–O–Ti bonds in solutions of diphenylsilanediol and titanium-tetra-isopropoxide. *J. Sol.-Gel Sci. Technol.* **6**, 139–149 (1996).
31. Crouzet, L., Leclercq, D., Mutin, P. H. & Vioux, A. Organosilsesquioxane–titanium oxide hybrids by nonhydrolytic sol–gel processes. Study of the rearrangement of Si–O–Ti bonds. *Chem. Mater.* **15**, 1530–1534 (2003).
32. Sosnov, E. A., Malkov, A. A. & Malygin, A. A. Hydrolytic stability of the Si–O–Ti bonds in the chemical assembly of titania nanostructures on silica surfaces. *Russ. Chem. Rev.* **79**, 907–920 (2010).
33. Bachmann, S. et al. Synthesis and solid-state NMR investigations of radiation-immobilized polysiloxanes on bare, titanium-grafted, and zirconium-grafted silicas. *Chem. Mater.* **13**, 1874–1879 (2001).
34. Rubinsztajn, S. et al. Reactions of titanium alkoxide with SiH containing polymers as a route to titanium/siloxane hybrid materials with enhanced refractive index. *Appl. Organomet. Chem.* **34**, e5571 (2020).
35. Wang, S. et al. Multifunctional polymer composite with excellent shear stiffening performance and magnetorheological effect. *J. Mater. Chem. C.* **2**, 7133–7140 (2014).
36. Evgeni, A. S., Malkov, A. A. & Malygin, A. A. Hydrolytic stability of the Si–O–Ti bonds in the chemical assembly of titania nanostructures on silica surfaces. *Russ. Chem. Rev.* **79**, 907 (2010).
37. Drozdov, A. D. & Dorfmann, A. The Payne effect for particle-reinforced elastomers. *Polym. Eng. Sci.* **42**, 591–604 (2002).
38. Chen, S., Fang, G., Qian, X., Li, A. & Ma, J. Influence of alkalinity and steric hindrance of lewis-base catalysts on atomic layer deposition of SiO_2. *J. Phys. Chem. C.* **115**, 23363–23373 (2011).
39. Prasad, D. & Mitra, N. Stereomutations in silicate oligomerization: The role of steric hindrance and intramolecular hydrogen bonding. *Phys. Chem. Chem. Phys.* **26**, 7747–7764 (2024).

40. Haenisch, J., Hinrichs, K. & Rappich, J. Surface functionalization toward biosensing via free-standing si-oh bonds on nonoxidized silicon surfaces. *ACS Appl. Mater. Interfaces* **11**, 31434–31440 (2019).
41. Zhuo, Y. et al. Simultaneously toughening and stiffening elastomers with octuple hydrogen bonding. *Adv. Mater.* **33**, 2008523 (2021).
42. Masuda, T. & Takagishi, H. Solution-processed aluminum metals using liquid-phase aluminum-hydrides. *J. Mater. Chem. C.* **8**, 14007–14014 (2020).
43. Zuo, F. et al. Self-doped Ti^{3+} enhanced photocatalyst for hydrogen production under visible light. *J. Am. Chem. Soc.* **132**, 11856–11857 (2010).
44. Scheiner, S. On the capability of metal–halogen groups to participate in halogen bonds. *CrystEngComm* **21**, 2875–2883 (2019).
45. Wang, X. et al. Electrosynthesis of ionic covalent organic frameworks for charge-selective separation of molecules. *Small* **18**, 2107108 (2022).
46. Ren, J., Li, Z., Liu, S., Xing, Y. & Xie, K. Silica–titania mixed oxides: Si–O–Ti connectivity, coordination of titanium, and surface acidic properties. *Catal. Lett.* **124**, 185–194 (2008).
47. Hoebbel, D., Nacken, M., Schmidt, H., Huch, V. & Veith, M. X-ray and NMR spectroscopic characterisation of cyclic titanodiphenylsiloxanes and examination of the hydrolytic stability of their Si–O–Ti bonds. *J. Mater. Chem.* **8**, 171–178 (1998).
48. Blandy, C., Pellegatta, J. L. & Gilot, B. Catalytic properties of supported titanates in transesterification. *J. Catal.* **150**, 150–154 (1994).
49. Deleuze, H., Schultze, X. & Sherrington, D. C. Polymer-supported titanates as catalysts for transesterification reactions. *Polymer* **39**, 6109–6114 (1998).
50. Chen, L., Xu, J., Xue, W. & Zeng, Z. Mechanism and kinetics of esterification of adipic acid and ethylene glycol by tetrabutyl titanate catalyst. *Korean J. Chem. Eng.* **35**, 82–88 (2018).
51. Ostanin, S. A., Kalinin, A. V., Bratsyhin, Y. Y., Saprykina, N. N. & Zuev, V. V. Linear/ladder-like polysiloxane block copolymers with methyl-, trifluoropropyl- and phenyl- siloxane units for surface modification. *Polymers* **13**, 2063 (2021).
52. Liu, Z. et al. Ultratough hydrogen-bond-bridged phosphorene films. *Adv. Mater.* **34**, 2203332 (2022).
53. Mizuno, K., Miyashita, Y., Shindo, Y. & Ogawa, H. NMR and FTIR studies of hydrogen bonds in ethanol-water mixtures. *J. Phys. Chem.* **99**, 3225–3228 (1995).
54. Tjandra, N. & Bax, A. Solution NMR measurement of amide proton chemical shift anisotropy in 15N-enriched proteins. Correlation with hydrogen bond lengths. *J. Am. Chem. Soc.* **119**, 8076–8082 (1997).
55. Crocker, M. et al. 1H NMR spectroscopy of titania. Chemical shift assignments for hydroxy groups in crystalline and amorphous forms of TiO_2. *J. Chem. Soc., Faraday Trans.* **92**, 2791–2798 (1996).
56. Zhao, C., Gong, X., Wang, S., Jiang, W. & Xuan, S. Shear stiffening gels for intelligent anti-impact applications. *Cell Rep. Phys. Sci.* **1**, 100266 (2020).
57. Romo, A. I. B. et al. Controlling charge percolation in solutions of metal redox active polymers: Implications of microscopic polyelectrolyte dynamics on macroscopic energy storage. *J. Am. Chem. Soc.* **146**, 17474–17486 (2024).
58. Dong, J. et al. Spontaneous molecule aggregation for nearly single-ion conducting sol electrolyte to advance aqueous zinc metal batteries: The case of tetraphenylporphyrin. *Angew. Chem. Int. Ed.* **63**, e202401441 (2024).
59. Lim, C. et al. Highly conductive and stretchable hydrogel nanocomposite using whiskered gold nanosheets for soft bioelectronics. *Adv. Mater.* **36**, 2407931 (2024).
60. Yuan, F. et al. A flexible viscoelastic coupling cable with self-adapted electrical properties and anti-impact performance toward shapeable electronic devices. *J. Mater. Chem. C.* **7**, 8412–8422 (2019).
61. Kresse, G. & Furthmüller, J. Efficiency of ab-initio total energy calculations for metals and semiconductors using a plane-wave basis set. *Comput. Mater. Sci.* **6**, 15–50 (1996).
62. Perdew, J. P., Burke, K. & Ernzerhof, M. Generalized gradient approximation made simple. *Phys. Rev. Lett.* **77**, 3865–3868 (1996).
63. Monkhorst, H. J. & Pack, J. D. Special points for Brillouin-zone integrations. *Phys. Rev. B* **13**, 5188–5192 (1976).
64. Chen, Z. et al. Supramolecular networks with high shear stiffening enabled by metal ion-mediated hydrogen bonding enhancement strategy. *Figshare* https://doi.org/10.6084/m9.figshare.29625734 (2025).
65. Li, X., Zhang, D., Xiang, K. & Huang, G. Synthesis of polyborosiloxane and its reversible physical crosslinks. *RSC Adv.* **4**, 32894–32901 (2014).
66. Wang, X., Zhang, Z., Liang, Z. & Yao, H. Hybridizing shear-stiffening gel and chemically-strengthened ultrathin glass sheets for flexible impact-resistant armor. *Adv. Sci.* **11**, 2403379 (2024).
67. Tang, M., Wang, W., Xu, D. & Wang, Z. Synthesis of structure-controlled polyborosiloxanes and investigation on their viscoelastic response to molecular mass of polydimethylsiloxane triggered by both chemical and physical interactions. *Ind. Eng. Chem. Res.* **55**, 12582–12589 (2016).
68. Zhao, C. et al. High-performance liquid metal/polyborosiloxane elastomer toward thermally conductive applications. *ACS Appl. Mater. Interfaces* **14**, 21564–21576 (2022).
69. Fan, T. et al. Multifunctional polyurethane composite foam with outstanding anti-impact capacity for soft body armors. *ACS Appl. Mater. Interfaces* **14**, 13778–13789 (2022).

Acknowledgements

This work was supported by the National Key R&D Program of China (2024YFA0920100 to R.H.), National Natural Science Foundation of China (22201296 to R.H.) and the Strategic Priority Research Program of the Chinese Academy of Sciences (XDB0930000 to X.-F.Y.).

Author contributions

Z.C., H.C. and R.H. contributed to the initiating idea. Z.C., H.C. and S.H.C. performed all the experiments. B.W. performed the computation method for the ESP and polymer chain intermolecular interaction calculations. Z.C., Y.L., Z.-Y.C., Q.H., X.-F.Y. and R.H. contributed to the data analysis and discussion. The paper was written by Z.C., H.C. and R.H. and edited by all the authors.

Competing interests

The authors declare no competing interests.

Additional information

Supplementary information The online version contains supplementary material available at https://doi.org/10.1038/s41467-025-64000-1.

Correspondence and requests for materials should be addressed to Rui He.

Peer review information *Nature Communications* thanks the anonymous reviewers for their contribution to the peer review of this work. A peer review file is available.